RADIATION RESEARCH **203**, 163–174 (2025)
0033-7587/25 $15.00

DOI: 10.1667/RADE-24-00244.1

Dose Build-up of High-energy ^{1}H and ^{4}He Ions in Standard, Innovative and In Situ Shielding Materials for Space Radiation: Measurements and Simulations

Francesca Luoni,[a,b,c] Uli Weber,[a,d] Alica Karin Lang,[a,b] Moritz Westermayer,[a,d,e] Felix Horst,[a,f] Marcello Baricco,[g] Luca Bocchini,[h] Martina Giraudo,[h] Giovanni Santin,[i] Christoph Schuy,[a] Marco Durante,[a,b] Daria Boscolo[a,1]

[a] Biophysics Department, GSI Helmholtzzentrum für Schwerionenforschung GmbH, Darmstadt, Germany; [b] Technische Universität Darmstadt, Darmstadt, Germany; [c] Current address: RP-AS Group, CERN, Meyrin, Switzerland; [d] Technische Hochschule Mittelhessen, Gießen, Germany; [e] CREATIS, CNRS UMR5220, University of Lyon, Villeurbanne, France; [f] OncoRay, National Center for Radiation Research in Oncology, Dresden, Germany; [g] Chemistry Department and NIS-INSTM, University of Turin, Torino, Italy; [h] Thales Alenia Space Italia, Torino, Italy; [i] ESA ESTEC, Noordwijk, Netherlands

Luoni F, Weber U, Lang AK, Westermayer M, Horst F, Baricco M, Bocchini L, Giraudo M, Santin G, Schuy C, Durante M, Boscolo D. Dose Build-up of High-energy ^{1}H and ^{4}He Ions in Standard, Innovative and In Situ Shielding Materials for Space Radiation: Measurements and Simulations. Radiat Res. 203, 163–174 (2025).

Galactic cosmic rays (GCR) are among the biggest hindrances to crewed space exploration. The ions contributing the most to fluence and absorbed dose in free space are ^{1}H and ^{4}He. In addition, their contribution to dose equivalent increases behind thick shields. In this work, the results of depth-dose measurements performed with high-energy ^{1}H and ^{4}He ions (2 GeV and 480 MeV ^{1}H, and 430 MeV/u ^{4}He) in structural (aluminum alloy), standard (PMMA and high-density polyethylene), innovative (lithium hydride) and in situ (Moon regolith simulant) shielding materials are presented. A strong dose build-up effect, due to target fragments and secondary protons, is observed in the first part of the Bragg curve for all the tested ion beams. The experimental results are compared to the Monte Carlo simulation tools most used for radiation protection in space, i.e., different physics lists of Geant4, PHITS, and FLUKA.

INTRODUCTION

The prolonged exposure of the human body to space radiation and the consequent biological effects are one of the major risks for human long-term missions in deep space and planetary habitats (*1–5*). Despite its limitations (*6*), passive shielding is currently the most promising radiation protection strategy (*1*, *2*, *7*).

Low-Z (low atomic number) materials are considered the best option for passive shielding purposes (*2*, *8–12*) and high-density polyethylene (HDPE) is commonly considered the gold standard for radiation protection in space (*2*, *9*). During the past decades, several experimental campaigns have been dedicated to testing the shielding capabilities of various materials (*10*, *13–21*). Most of them were performed with ^{56}Fe ions, and only a few with light ions. However, the main contributors of GCR to fluence and dose in free space are ^{1}H and ^{4}He ions (*2*). The energy spectra of ^{1}H-ions peak around 500 MeV for solar minimum and 1 GeV for solar maximum, while the one of ^{4}He ions peaks around 200 MeV/u for solar minimum and 500 MeV/u for solar maximum (*22*). In addition, the relative contribution of such ions to the blood-forming organ dose equivalent increases from 10% in free space, up to around 70% in a 30 g/cm^2 aluminum sphere (*23*, *24*). An accurate knowledge of the processes underlying their dose deposition is, therefore, required for radiation transport codes and risk assessment models.

While the dose equivalent is a significant parameter for radiation protection and inverse shielding effects, nonetheless, dose equivalent and radiation quality have been demonstrated for several space-relevant shielding materials (*25–27*). Depth-dose curves represent a useful benchmark for radiation transport codes and, at the same time, allow a direct comparison of the shielding efficacy of different materials. Similar approaches have been used by several investigators (*15*, *18*, *28*).

In this work, experimental depth-dose distributions in targets relevant to space radiation shielding applications (aluminum, polyethylene, PMMA, lithium hydride, and Moon regolith simulant) are presented for 2 GeV and 480 MeV ^{1}H beams and a 430 MeV/u ^{4}He beam. A particular focus is placed on the entrance region where large build-up effects, extending up to several tens of g/cm^2 of target thickness, are observed. When crossing a target, nuclear interactions occur between the beam and the target creating a spectrum

[1] Corresponding author: Daria Boscolo, Biophysics Department, GSI Helmholtzzentrum für Schwerionenforschung GmbH, Darmstadt, Germany; e-mail: d.boscolo@gsi.de.

TABLE 1
List of the Ion Beams, Energies, Beam Sizes (full-width-half-maximum FWHM), Target Materials, and Facilities of the Experiments

Ion	Energy	FWHM	Targets	Facility
^{1}H	2 GeV	$\sim$ 20 mm	PMMA, LiH	GSI
^{1}H	480 MeV	$\sim$ 5 mm	HDPE, LiH, aluminum alloy, Moon regolith simulant	HIT
^{4}He	430 MeV/u	$\sim$ 5 mm	HDPE, LiH, aluminum alloy, Moon regolith simulant	HIT

of low-energy particles that varies depending on the primary beam particles, the beam energy, and the material of the target. In the case of proton beams, only fragmentation of the target can take place. These secondary particles typically have short ranges (in the order of tenths of microns for the heavy fragments, up to a maximum of a few centimeters for the light ions) and increased linear energy transfer (LET). They, therefore, contribute strongly to the local dose deposition, especially in the entrance channel. Data on nuclear build-up effects have been published in the literature for proton beams both in therapy (*28*, *29*) and in space radiation (*15*, *20*, *30*, *31*) energy range, but only for a few target materials and, to our best knowledge, only for proton and helium beams. This study focuses on secondary charged particle production. Dedicated studies focusing on neutron production for the same beams, shielding materials, and similar experimental conditions have also been carried out but are presented in a separate publication (*32*).

The experimental data presented in this work are divided into two parts, as they were acquired in two independent experimental campaigns and with slightly different experimental setups. The measurements for the 480 MeV ^{1}H and 430 MeV/u ^{4}He beams were performed at Heidelberg Ion Therapy Center (HIT) as part of the European Space Agency, Continuously Open Research Announcement Investigating Biological Effects of Space Radiation (ESA-CORA-IBER) project named DosE build-up Measurement of energetic proton and helium ions for space radiation Shielding applications (DEIMOS). The data for 2 GeV ^{1}H were obtained in the medical vault of GSI (Cave M) within the context of the ESA-funded project ROSSINI3.

Monte Carlo simulations have also been performed for all experimental scenarios. In particular, the 2 GeV ^{1}H-beam data were compared with the outcomes of commonly used Monte Carlo codes for radiation protection in space purposes, i.e., FLUKA (*33–36*), PHITS (*37*, *38*) and Geant4 (*39–41*) These codes were also compared to previous ROSSINI3 experimental campaign results (*18*). Simulations for the 480 MeV ^{1}H and 430 MeV/u ^{4}He data sets have been performed using only the FLUKA code. This code showed suitable performance for the 2 GeV ^{1}H data presented in this work, lower Z material results for the case of 1 GeV/u ^{56}Fe ions (*18*), and was already proven to reproduce the proton dose build-up in the therapeutic region. Additionally, the code was recently improved for ^{4}He ions on ^{12}C and ^{16}O targets, in the therapeutic energy range (*42–44*).

MATERIALS AND METHODS

Depth-dose curve measurements of the structural (aluminum alloy), innovative [lithium hydrid (LiH)], standard (HDPE and PMMA), and in situ (Moon regolith simulant) shielding materials, have been performed with 480 MeV ^{1}H and 430 MeV/u ^{4}He beams at HIT and a 2 GeV ^{1}H beam in the GSI Cave M. An overview of the experimental campaigns and a description of the ion beams used are shown in Table 1. Detailed descriptions of the experimental setups, target materials, and Monte Carlo simulation approaches can be found below.

Target Materials

LiH appears to be very promising shielding material from heavy ions during interplanetary flights. This material has already proven to offer an optimal compromise between shielding performances and costs of the material mass load (*19*, *21*). In this work, LiH pellets were prepared starting from powder, with a purity higher than 97% (Alfa Aesar; CAS number: 7580-67-8). A suitable amount of hydride powder was loaded into a mold, which progressively pressed up to 13 tons, leaving it under a maximum pressure for 5 min. The mold was moved to a lab glove box to extract the pellet. The sample was then weighed and measured. Finally, the pellet was packaged in a sealed bag to prevent contact with moisture. Similar targets were used in a series of experimental setups in the context of the ESA-founded ROSSINI projects (*15*, *16*, *18*). In this work, 14 LiH cylindrical pellets with a diameter of $\sim$6.5 cm and a total thickness of 8.56 g/cm^2 were used. Different from the other investigated materials, in the case of the LiH, only the initial part of the build-up region was investigated. Due to the small lateral dimensions of the LiH targets, the addition of more targets would have resulted in a loss of absorbed dose outside of the IC2 area due to lateral scattering. This was tested through Monte Carlo simulations before the experimental campaign took place. Details about the material dimensions and densities can be found in Table 2, while target production and characterization have been described elsewhere (*18*).

Moon regolith simulant. The use of in situ material can represent a practical strategy to build permanent or semi-permanent habitats on the Moon. The abundance of material and the minimized transport costs would allow the construction of very thick shields against cosmic radiation. In this work, the OPRH2N Near-Side Highland Lunar regolith simulant from Off Planet Research (https://www.offplanetresearch.com/) was used for depth-dose curves measured at HIT. This target material has already been used in different experimental and simulation studies (*18*, *45*). It consists of sand grains with a diameter between 250 and 500 μm, and its composition is reported in Table 3. The simulant was irradiated inside PMMA containers with a lateral area of 25 $\times$ 25 cm^2, and a thickness of 11 cm. One box was 6 cm thinner, to allow for a finer depth resolution. The box wall thickness was 0.5 cm on each side.

Aluminum alloy. Aluminum is one of the main structural components of spacecraft. In this work, plates made of an aluminum alloy with 3% (weight fraction) magnesium in aluminum were used. The plates have a lateral area of 30 $\times$ 30 cm^2 and thicknesses of 20 mm, 25 mm, and 30 mm were used as target materials. The alloy composition is provided in Table 4, while the density and target characterization are provided in Table 2.

HDPE and PMMA. High-density polyethylene (HDPE) is the gold standard for space radiation protection and was often used in

TABLE 2
List of the Materials Used for the Irradiations, Alongside Their Mass Densities (ρ), Areas Perpendicular to the Beamline (A), and Maximum Irradiated Thickness (t_{max})

Material	ρ (g cm^{-3})	A (cm^2)	t_{max}[a] (g cm^{-2})
LiH (ROSSINI3)	0.5279 (48)	33.20 (51)	3.096 (29)
LiH (DEIMOS)	0.5279 (48)	33.20 (51)	8.56 (6)
PMMA	1.183 (11)	400.300 (60)	37.004 (97)
HDPE	0.9340 (96)	900 (2)	112.62 (33)
Moon regolith simulant	1.345 (91)[b]	625 (20)	169 (3)
Aluminum alloy	2.6674 (19)	900.0 (4)	148.089 (54)

Notes. The thicknesses are given in areal densities. In parentheses, the associated uncertainties are reported. They apply to the least significant digits.

[a] The maximum areal density includes several additional materials in the beamline, e.g., protection plate, PMMA layers of the Moon boxes, and plastic bag layers for LiH.

[b] The Moon regolith simulant was stored and irradiated in PMMA boxes with a lateral area of 25 × 25 cm^2. Nevertheless, the boxes were not filled to the top due to practical reasons, therefore the large uncertainty.

experimental campaigns as a comparison (*2*). In this work, a series of plates with a thickness of 5 cm or 10 cm and a lateral area of 30 × 30 cm^2 was used to measure the full depth-dose distribution of the 480 MeV ^{1}H and 430 MeV/u ^{4}He beams. PMMA plates of 20 × 20 cm^2 have been used to measure the build-up region for the 2 GeV ^{1}H beam, for a maximum areal density of 37.004 ± 0.097 g/cm^2.

Experimental Setup

Schematics of the experimental setups for the HIT and GSI experiments are shown in Fig.1a and b, respectively. The HIT setup consisted of variable target thicknesses placed in between two large-area ionization chambers (ICs). The closest to the beam exit window (here referred to as IC1) was operated as a reference monitor for normalization. In this way, the results were not affected by unavoidable fluctuations in the beam intensity. The second chamber (here referred to as IC2) was placed after the target and used to measure the energy loss after the target, which is proportional to the dose at this thickness. The target material was stacked as close as possible to the IC2 to minimize beam widening due to scattering effects, leading to dose deposition outside the sensitive volume of the ionization chamber.

The charge readout of the ionization chambers was realized with high-precision electrometers (model 6517b, Keithley). This is our GSI internal standard technique for precise depth-dose distribution measurements and very similar setups have been used in the past (*15*, *16*, *18*, *28*, *46–48*). In the cases where the full dose deposition curves were measured, the fine steps around the Bragg peak position were obtained by using the so-called range shifter.

TABLE 3
Highland Moon Regolith Mass Percentage Composition

Element	Mass contribution (%)	Element	Mass contribution (%)
SiO_2	47.89	Al_2O_3	27.06
Ti O_2	0.52	FeO	3.68
MnO	0.06	MgO	2.84
CaO	14.19	Na_2O	2.43
K_2O	0.25	P_2O_6	0.2
LOI	0.88		

Note. LOI stays for low order.

TABLE 4
Aluminum Alloy Average Mass Percentage Composition

Element	Mass contribution (%)	Element	Mass contribution (%)
Al	94.2 ÷ 97.4	Cr	<0.3
Cu	<0.1	Fe	<0.4
Mg	2.6 ÷ 3.6	Mn	<0.5
Si	<0.4	Ti	<0.15
Zn	<0.2	LOI	<0.15

Note. LOI stays for low-order impurities.

This device consists of a set of thin foils and plates with well-defined areal densities, each roughly doubling the previous one in thickness. Being remotely controlled, this device allows quick changes in the amount of material in the beam path. In the case of the polyethylene and Moon regolith simulant depth-dose distributions, the range shifter was equipped with polyethylene plates, while in the case of aluminum-alloy depth-dose measurements, a set of plates made of the same aluminum alloy were used in the range shifter. For the GSI measurements, the setup was almost identical, except for the range shifter, which was not used, and a third large area parallel plate IC (IC3) was placed right upstream of the target material to measure the dose deposited by backscattered particles.

The protection plates reported in Fig. 1 are 0.4875 cm thick and made of PMMA. The only exception was aluminum-alloy measurements, for which the IC2 protection plate facing the target was made of aluminum. The thickness of this plate is 0.5 mm.

Data Analysis

The laterally integrated depth-dose distributions were obtained from the ratio of the signals collected by the two ICs as a function of the target thickness. The values presented are normalized to the no target value as described in Eq. (1):

$$\frac{D_2}{D_1} = \frac{Q_2/Q_1}{Q_{2,\,no\,target}/Q_{1,\,no\,target}} \quad (1)$$

An accurate description of the error calculation and data analysis process can be found in greater detail elsewhere (*18*).

480 MeV ^{1}H and 430 MeV/u ^{4}He Beams at HIT Monte Carlo Simulation

The results of the HIT experimental campaign were compared with the FLUKA code (version 2021.2.3), in combination with the graphical user interface flair (version 2.3-0). The simulations were performed with 5 × 10^6 primary particles to keep the uncertainty below 1% and using the PRECISION DEFAULTS card. Transport cuts for e$^-$ and γ were set to 100 keV, as the delta ray production cut. Projectile and target electromagnetic dissociation and coalescence processes were activated.

The beam momentum distribution was assumed to be Gaussian and set at $\Delta p/p = 10^{-3}$ for both ion beams. The beam shape was assumed to be Gaussian with full-width-half-maximum in the x and y-directions as given in Table 1. The full experimental setup was simulated according to the schematic shown in Fig. 1(a). The HIT beam nozzle, which consists of several ionization chambers and two multi-wire proportional chambers, was substituted with a water thickness of 1.7 mm.

ICs were described with an active gas layer 2 cm of 80% Ar/20% CO2 mixture, surrounded by 1 cm air and a 2.5 μm thick Mylar foil per side. The gas density was calculated from its molar mass and set to 1.694 × 10^{-3} g/cm^3. The USRBIN scorer type was used to score the dose in the regions filled with ArCO2. The AUXSCORE card was also used to score the dose contribution of all fragments.

The compositions and properties of the target material were established as described in Materials and Methods. For the complex targets,

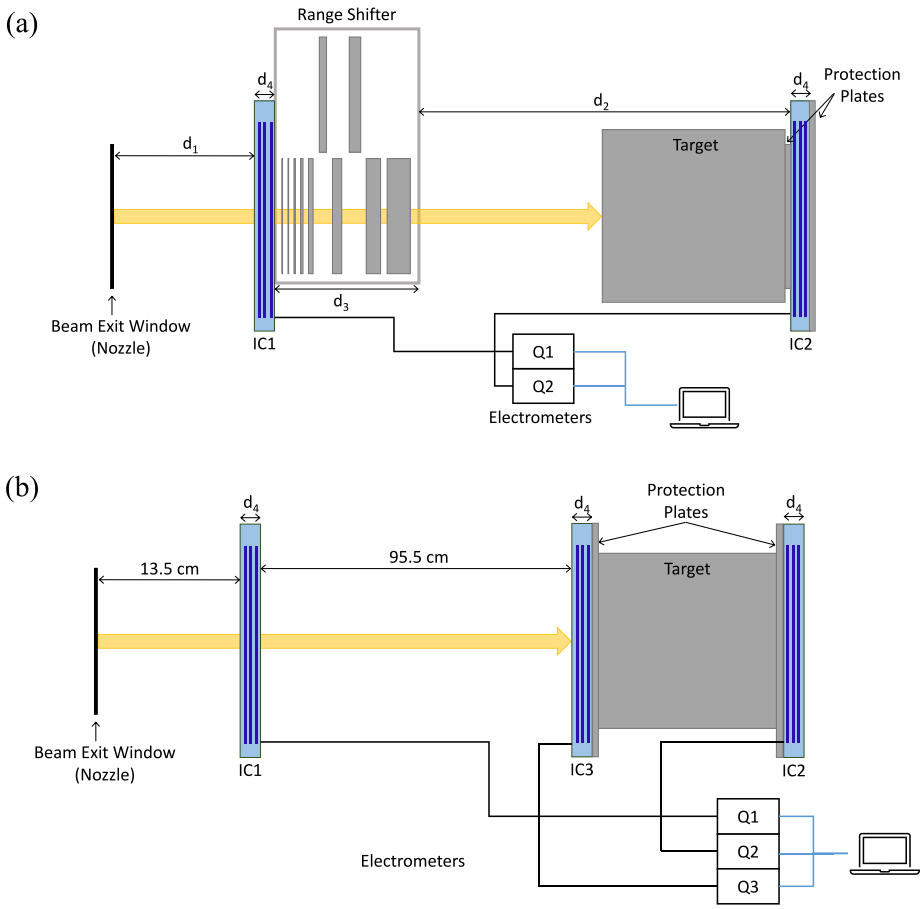

FIG. 1. Schematics of the experimental setups used at HIT (panel a) and GSI (panel b). d1 = 12.3 cm for the aluminum alloy and 26.5 cm for HDPE, LiH and Moon regolith simulant, d2 = 107.2 cm for the aluminum alloy and 135 cm for HDPE, LiH and Moon regolith simulant, d3 = 35.6 cm, and d4 = 4 cm.

such as the LiH and Moon regolith simulant, the support materials (consisting of the plastic bags and support plates for the LiH and the PMMA boxes for the Moon simulant) were also included in the simulation.

A modification was made to the properties of the FLUKA standard polyethylene material: The I value was changed from 57.4 eV (the standard in FLUKA) to 64.6 eV. This modification helped reduce an 11% relative shift in the Bragg peak position, which was initially observed between the experimental and simulated data. The value of 64.6 eV is also in agreement with the polyethylene I-value obtained from depth-dose data with uranium ions (*48*). This value has been used for the simulations whose results are reported in this work. This is valid for both the HDPE target and for the HDPE plates placed in the range shifter.

2 GeV ^{1}H Beam at GSI Monte Carlo Simulation

Simulations reproducing the experimental GSI campaign (2 GeV proton beam) have been carried out using the Monte Carlo particle transport codes PHITS (version 3.20), Geant4 (version 10.6 patch-02), and FLUKA (version 2020.0.3) in combination with the graphical user interface flair (2.3-0). For the Geant4 simulations, different physics lists have been tested: QGSP_INCLXX, QBBC_EMY, and FTFP_BERT. In all simulations, the number of primary ions generated has always been selected high enough to decrease the statistical errors to less than 3% (10^4 to 10^5 ions).

The beam was modeled with a Gaussian shape with 2-cm full width-half maximum (FWHM) and no divergence. In the PHITS and Geant4 simulation setups, the ICs were filled with the actual $ArCO_2$ mixture with no detailed internal electrode structures. The dose was scored in the active regions of the two ICs: In Geant4 the dose was calculated by summing up the energy deposition in the scoring volumes and dividing it by the mass, while in PHITS, t-deposit tally was used. In PHITS, a 1.0×10^{-3} MeV energy cut has been used for electrons, gamma rays, and positrons, while the production threshold for delta rays was set to 0.1 MeV. In Geant4, the default range cut of 0.1 mm was used. The FLUKA simulations were run with the same parameters as described for the 480 MeV ^{1}H beam.

RESULTS AND DISCUSSION

Dose-Ratio Experimental Data

480 MeV protons and 430 MeV/u helium ions. In Figs. 2 and 3, the experimental depth-dose profiles are shown for 480 MeV proton and 430 MeV/u ^{4}He beams, respectively.

For all targets, a strong build-up effect is observed in the first part of the curves. It reaches a maximum between 14–15 g/cm^2 for HDPE and Moon simulant and 21 g/cm^2 for aluminum alloy. An increase in the dose ratio of up to 35% for protons and 23% for He ions was measured. This effect is mostly due to the target fragments and secondary protons. They have low energy and high LET. Therefore, they contribute strongly to the local dose deposition, especially in the first g/cm^2. The depth of the dose build-up effect is proportional to the range of such particles in the

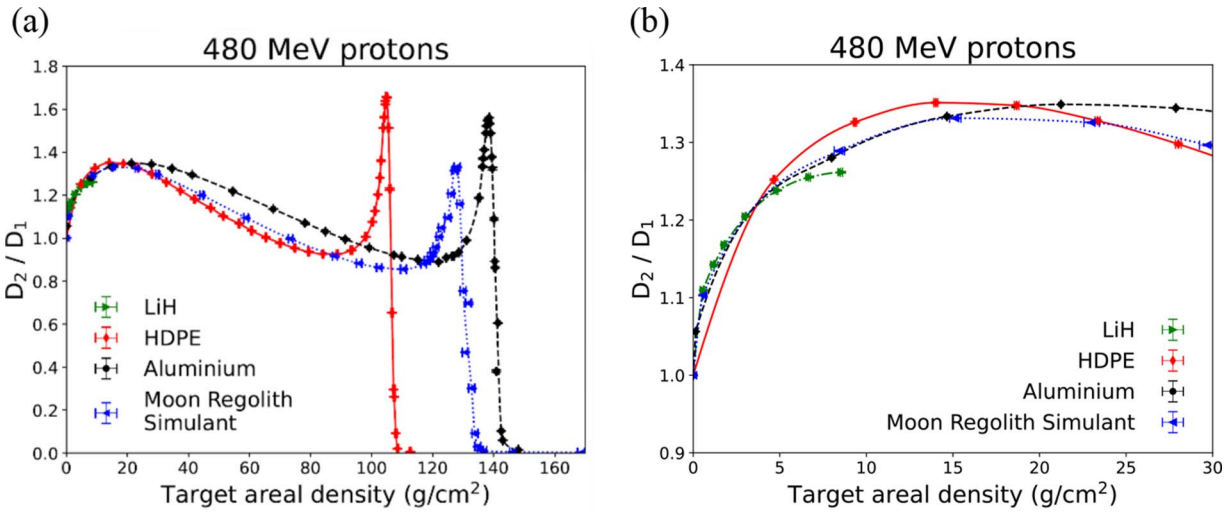

FIG. 2. Experimental depth-dose distribution curves obtained with 480 MeV protons. Panel a shows the full Bragg curves in the aluminum alloy, HDPE, Moon, regolith simulant and LiH. Panel b is a zoom-in. The dashed lines connect the experimental points.

target material. The build-up reaches a maximum at a depth where the projectile fragmentation takes over and the dose ratio starts to decrease.

As shown in Figs. 2 and 3, the depth-dose distribution of the aluminum alloy, HDPE, and Moon regolith simulant is similar in the build-up region, suggesting that the production of secondary particles is quite similar in the three materials. However, it must be considered that the Moon regolith simulant was irradiated inside PMMA boxes. For both the beams, instead, the LiH target shows a weaker build-up compared to the other investigated materials. Monte Carlo simulations were performed to investigate this effect in detail. Their results suggest that this effect is likely due to the secondary particles laterally escaping the target volume (*49*). The Bragg peak position is different for the three target materials because of their different electron density: $1/\rho$ energy loss per unit pathlength $(dE/dx) \propto Z_T/A_T$.

When comparing proton and helium depth-dose distributions (see Fig. 4), it can be observed that the build-up is higher for the proton beams. This is due to the higher dE/dx of helium ($dE/dx \propto Zp^2$), which increases the entrance channel and makes the relative contribution of the secondary particles smaller, combined with the fragmentation of the primary ions, which pulls the depth-dose curve down because of the lower dE/dx of the secondary particles. Additionally, in Fig. 4d, the results obtained with LiH and the 2 GeV proton beam are also reported. For higher proton beam energies, the build-up effect is also stronger. This can be explained again by a reduced stopping power of the more energetic proton beam ($dE/dx \propto vp^{-2}$) and, thus, a larger relative contribution to the energy deposition of the secondary fragments produced via nuclear interaction. The ranges of ^{4}He ions are shorter because of the lower kinetic energy per nucleon of the beam.

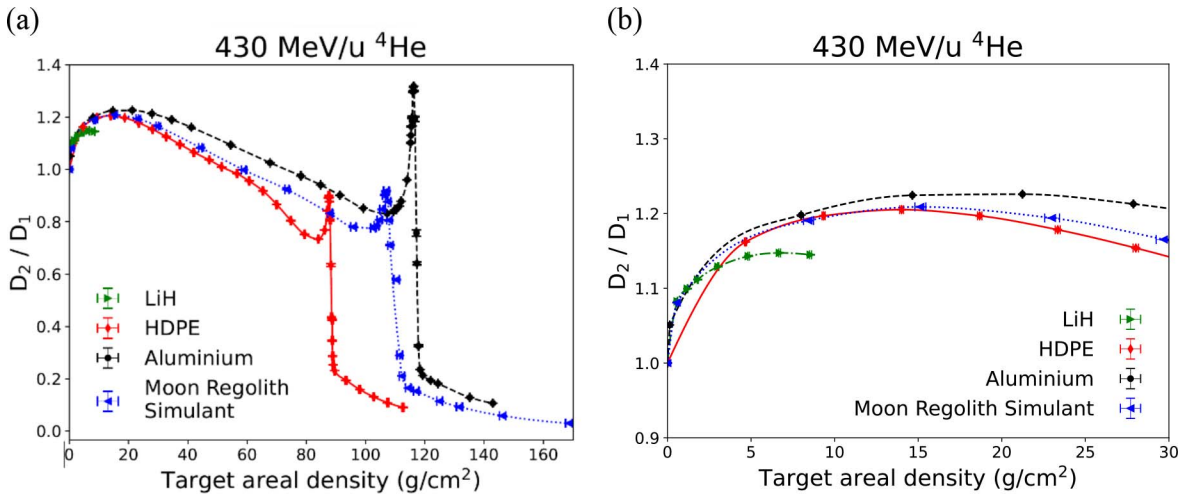

FIG. 3. Experimental depth-dose distribution curves obtained with 430 MeV/u ^{4}He ions. Panel a shows the full Bragg curves in the aluminum alloy, HDPE, Moon, regolith simulant and LiH. Panel b is a zoom-in. The dashed lines connect the experimental points.

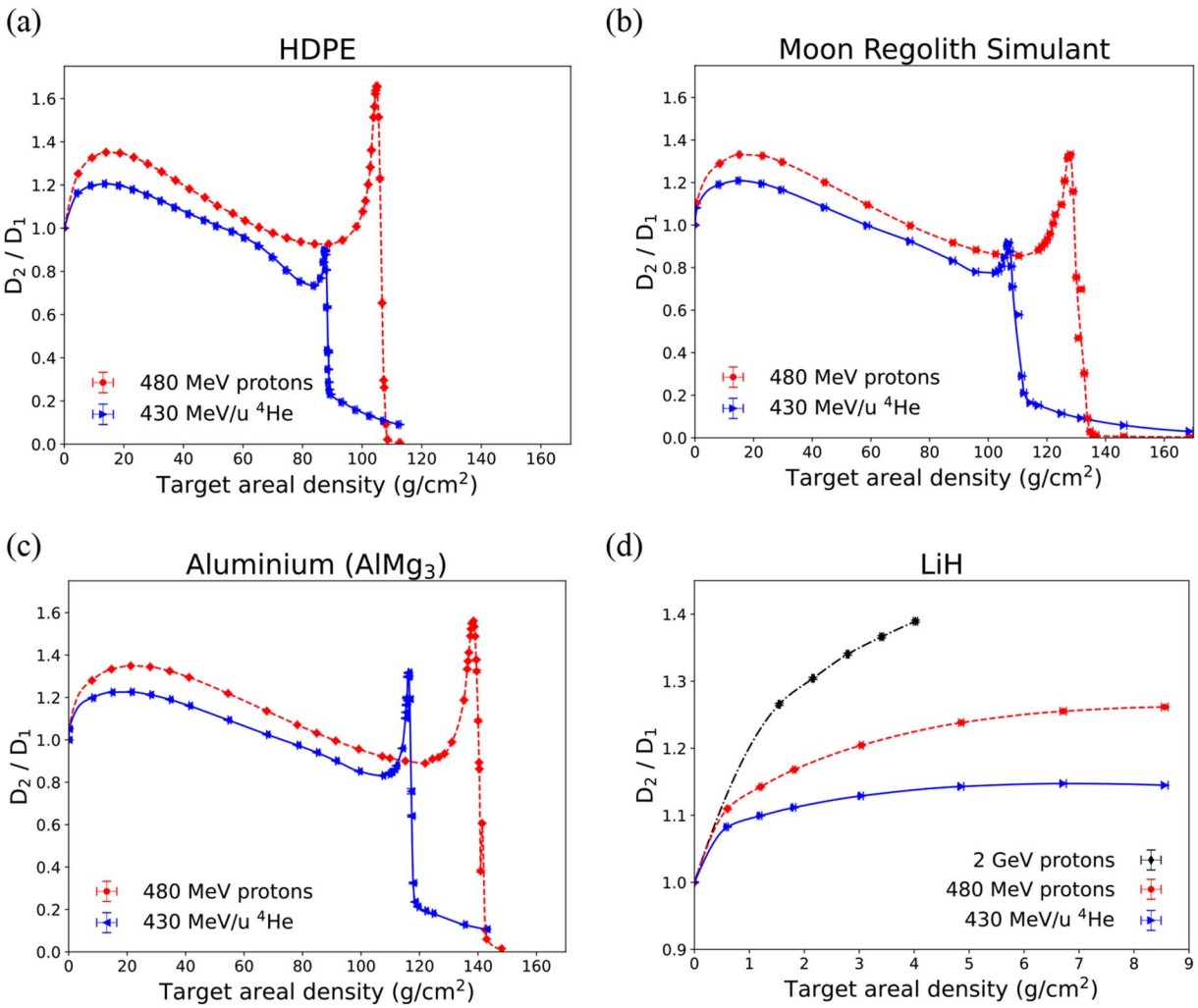

FIG. 4. Same results of Figs. 2 and 3 plotted by grouping the curves by target: HDPE data (panel a), Moon regolith simulant (panel b), the aluminum alloy (panel c) and LiH (panel d). The dashed lines connect the experimental points.

2 GeV protons. The dose ratios obtained with 2 GeV proton beams at GSI, Fig. 5 shows the two target materials used in this experimental campaign, i.e., PMMA, and LiH. Figure 5a shows a very strong build-up effect can be observed for both target materials, reaching a maximum of 80% dose increase for the PMMA between 25 and 30 g/cm^2. Because of the reduced measured thicknesses (up to only 4 g/cm^2) of the LiH target, the maximum of the build-up was not reached. However, from the trend shown by the measurements in the first g/cm^2 of LiH, a lower build-up maximum is expected for LiH compared to PMMA.

As discussed in the Experimental Setup section, a third ionization chamber (IC3) was placed in front of the target to measure the dose increase due to the electrons and nuclear fragments emitted in the backward direction (see Fig. 1). The results obtained with IC3 are shown in Fig. 5b. For the PMMA, an increase up to 12% is observed in front of the target in the first 20 g/cm^2, after which a plateau is reached. This means that only the first layers of the target material contribute to the backscattered dose, while the electrons and nuclear fragments produced at deeper locations get reabsorbed within the target itself before reaching the edge. This is due to the relatively short ranges of most of these backward-directed secondary particles, which are presumably produced mostly through nuclear evaporation. A similar trend is shown by the LiH, where a dose increase of approximately 6% is observed in the first 4 g/cm^2.

Comparison with Monte Carlo Simulations

480 MeV protons. Figure 6 shows the comparison between the simulation results and experimental dose ratios for the 480 MeV/u ^{1}H ion beam. Together with total dose distribution, the contribution of protons and secondary target fragments is also shown. To distinguish between the impact of primary protons and protons originating from nuclear interactions, the curve for beam-particle dose is displayed alongside the total proton dose. A good agreement between the simulated and experimental data was found, confirming the transport models in FLUKA for 480 MeV protons.

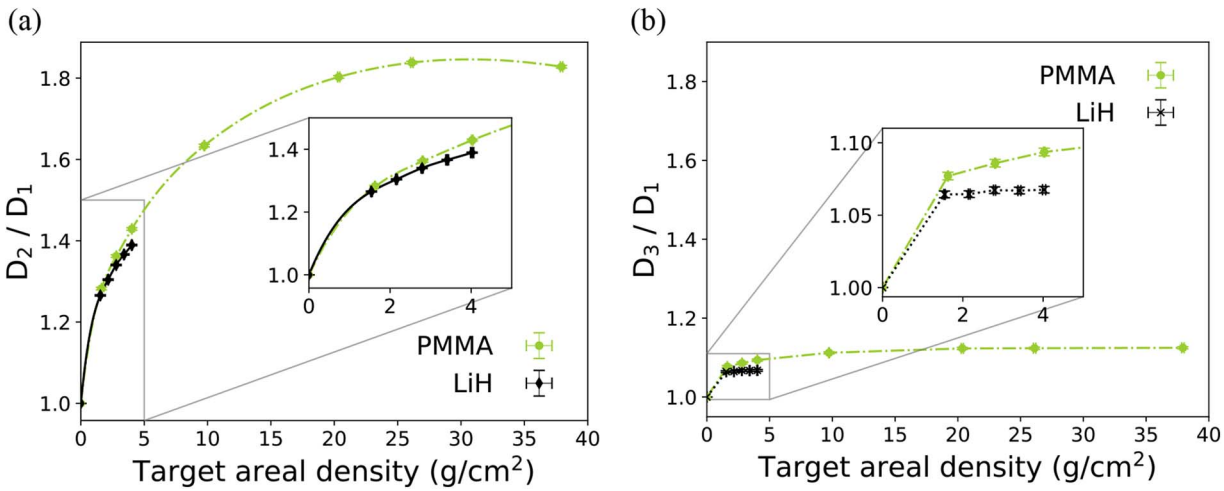

FIG. 5. Dose buildup (D_2/D_1 and D_3/D_1) of 2 GeV protons in PMMA and LiH.

The build-up region is very well reproduced by FLUKA in all the investigated materials with deviations of less than 5%. For the targets with which the full depth-dose distribution curves were measured, the Bragg-peak positions were matched with a 1% accuracy after previously described modifications to the FLUKA standard PE I-value. For the aluminum-alloy and Moon-simulant targets (Fig. 6b and c), an overestimation of the predicted FLUKA dose is observed

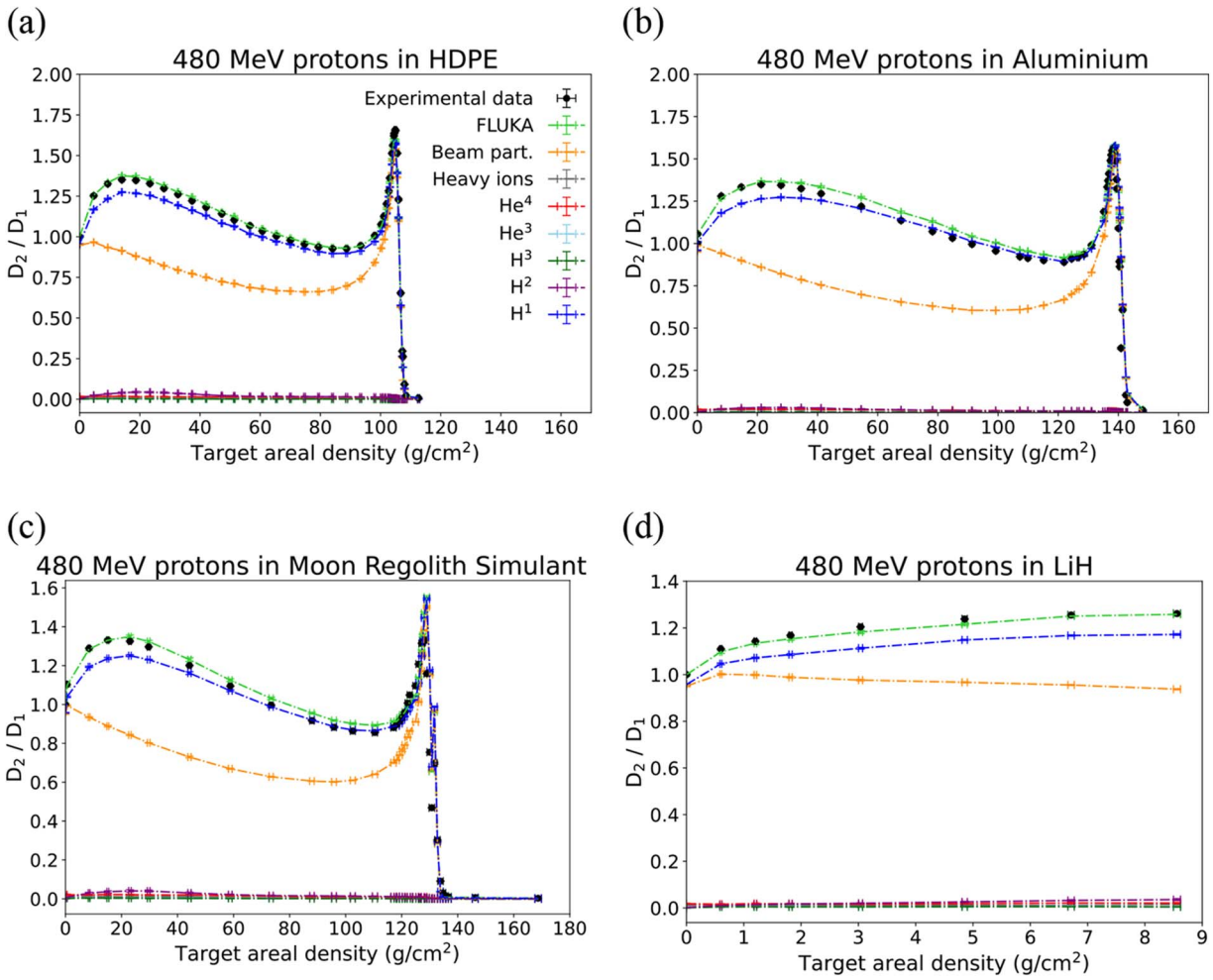

FIG. 6. Comparison between experimental points and FLUKA simulation outcomes for the 480 MeV/u ^{1}H ion beam.

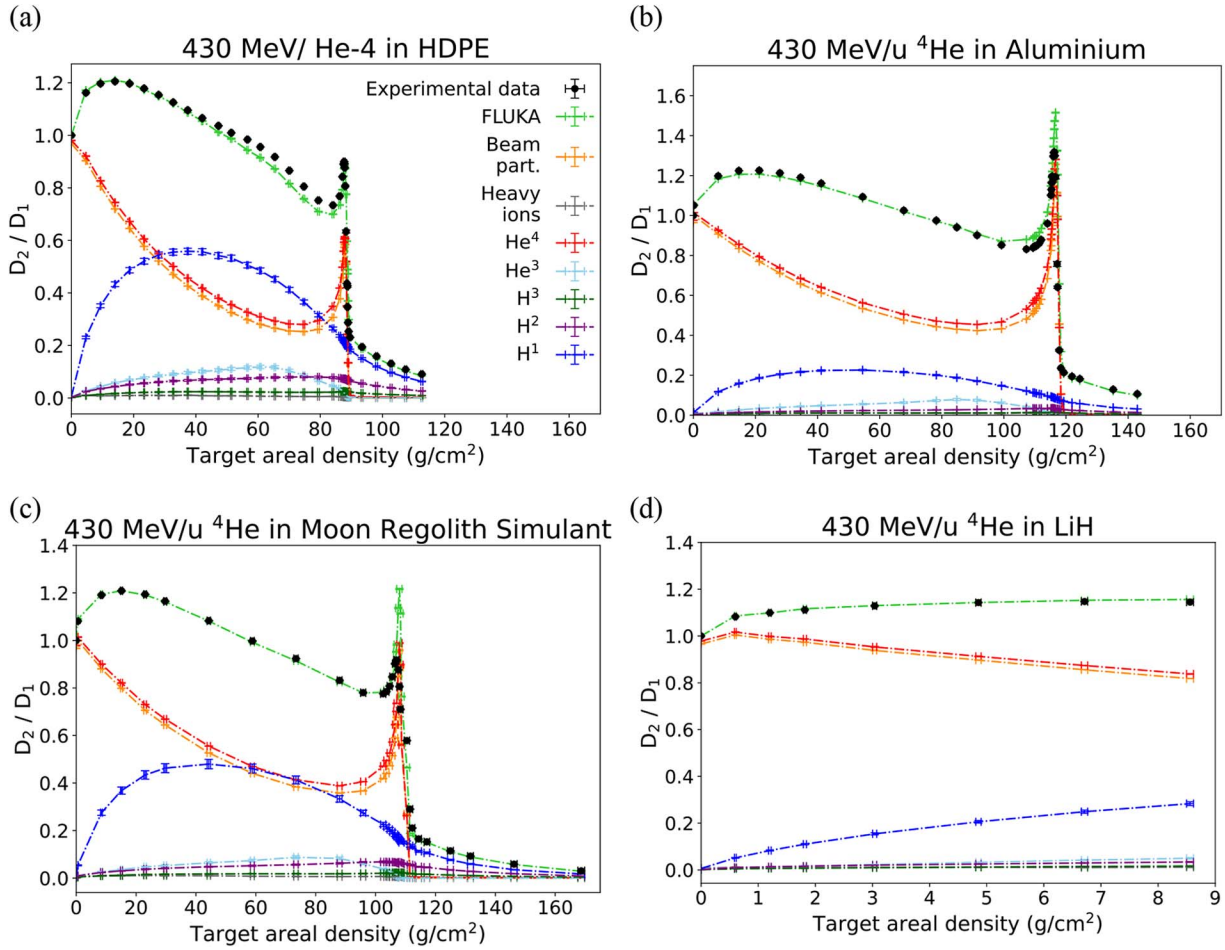

FIG. 7. Comparison between experimental points and FLUKA simulation outcomes for the 430 MeV/u ^{4}He ion beam. The Monte Carlo-predicted contribution of the single fragments is also given for each target material.

in the central region of the depth-dose distribution curve. This effect can be due to an underestimation of the lateral scattering in FLUKA. If the predicted angular spread is smaller than a larger number of ions (which are laterally scattered outside of the target) reach the IC2 and increase the dose D_2 in the simulations. This effect is expected to be larger in heavier targets and with lighter ions (*50*), which would explain why it is not observed in HDPE and for helium ions. This hypothesis is also supported by additional simulations where the effect is reproduced by reducing the sensitive area of the IC2 in the FLUKA geometry from a surface of 26 × 26 cm^2 to a chamber size of 20 × 20 cm^2 (*49*). It could also be due to double-differential nuclear cross-sections that overestimate the production angle of secondaries. In the case of the Moon-simulant target (Fig. 6c), the simulated Bragg peak is about 22% higher and it is also sharper than measured. This effect is most probably due to inaccuracies in the material description in FLUKA, i.e. in the Monte Carlo simulations, the granularity and density inhomogeneities in the Moon sand are not accounted for.

430 MeV/u helium ions.. Figure 7 shows the comparison between simulation and experimental data, alongside the simulated fragment contribution to the dose deposition. For all targets, protons are the main contributor to the dose build-up, exceedingly even the dose contribution from the primary helium beam in some regions of the HDPE curve (see Fig. 7a). Due to the higher relative importance of fragmentation cross-section to dE/dx for the low-Z materials, the secondary fragment production is larger for HDPE and significantly reduced in the aluminum alloy. In the case of the Moon simulant, the non-negligible amount of PMMA in the containers also contributes significantly to the production of proton and light fragments. Overall, a very good agreement between the measured curve and the FLUKA simulation is found with deviations lower than 2% in the buildup region for all the targets investigated. Also, the Bragg peak position matches within 1% for all targets where the full depth-dose distribution has been measured. Similar to what is observed in the proton experiment, in the Moon simulant target the predicted dose in the Bragg peak is 30% higher compared to the measured values, Fig. 7c. As already mentioned, this can be due to density inhomogeneities deriving from the fact that the Moon target is sand. Additionally, this can be explained as the optimization of the Tripathi nuclear cross-section model was implemented in FLUKA for ^{12}C

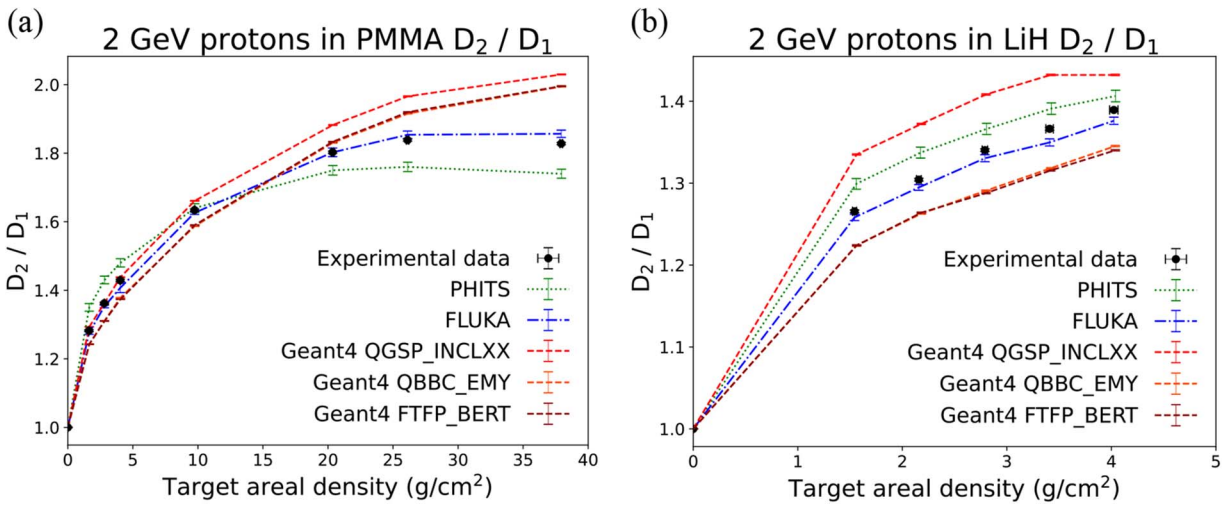

FIG. 8. Comparison between D_2/D_1 experimental data and Monte Carlo simulation results for PMMA and LiH irradiated with the 2 GeV ^{1}H beam.

and ^{16}O targets only (*42*, *43*), and not for heavier targets (*44*, *51*). It was highlighted that this model, which is used within FLUKA, cannot match the experimental cross-section data for these combinations of projectile and targets (*44*, *51*, *52*).

The same holds valid for the aluminum alloy targets, as the FLUKA predicted dose ratio in the Bragg peak area is 20% higher than the measured values (Fig. 7b). In this case, deviations are also observed in the entrance channel, where the FLUKA prediction slightly underestimates the doses, and in the region proximal to the Bragg peak, where the simulated dose is a bit higher than the measured one. These observations might point to a slight underestimation of the primary ion fragmentation cross-sections (*44*, *51*) as more helium ions would contribute to the dose in the Bragg peak. An optimization of the Tripathi model to match aluminum targets has been published previously (*51*).

In the case of HDPE, target deviations are observed in the region between 45 g/cm^2 and 80 g/cm^2 with a maximum relative deviation of 5.81% (Fig. 7a). A likely explanation for the observed deviation is an underestimation of the ^{3}He fragment production. Its position matches the expected average range of the ^{3}He fragments [$\sim$3/4 of the primary beam range (*47*)] and is the region where the dose contribution of the ^{3}He fragments is the maximum. ^{3}He production cross-sections for ^{4}He projectiles on HPDE that can be used to optimize nuclear models have been published previously (*44*).

Comparison with Monte Carlo Simulations: 2 GeV Protons

Monte Carlo simulations of the 2 GeV ^{1}H-beam are reported in Fig. 8 for D_2/D_1 and in Fig. 9 for D_3/D_1. For this data set, several different Monte Carlo codes were used, namely FLUKA, PHITS, and Geant4. Three different Geant4 physics lists were used, namely QBBC_EMY and FTFP_BERT and QGSP_INCLXX. The error bars of the simulation results are the statistical deviations of the Monte Carlo. FLUKA is the code that provides the best overall agreement. It closely reproduces the experimental data of the depth-dose distributions for both target materials. It only slightly underestimates the predictions for backscattered dose build-up in LiH (Fig. 9b). Our data agrees with what was observed in previous findings (*18*).

The PHITS code overestimates the measured values in all cases, except for PMMA (Fig. 8a), where it predicts a slightly shorter and lower build-up. Geant4 results are strongly affected by the chosen physics lists. In particular, the QGSP_INCLXX list always overestimates the measured data, while the QBBC_EMY and FTFP_BERT lists overestimate the experimental values for PMMA and underestimate them for LiH. The results obtained with QGSP_INCLXX are quite surprising. Contrary to previous studies with iron beams (*18*), where the Geant4 physics lists better reproducing the experimental data, it overestimates both the knockout of secondary protons (D_2/D_1 results) and the production of evaporation nucleons (D_3/D_1 results). This might suggest that the Leige Intranuclear Cascade model for low energies used in QGSP_INCLXX reproduces well the evaporation results of a nuclear fragmentation interaction undergone by a high-energy heavy projectile such as iron, but not of a spallation reaction of a high-energy proton.

CONCLUSION

Absorbed depth-dose distribution measurements for high-energy light-ion beams were performed in well established (aluminum, PE and PMMA), innovative (LiH), and in situ (Moon regolith simulant) materials for long-term deep-space exploration. These beams are the main GCR contributors to fluence, absorbed dose in free space, and dose equivalent in blood-forming organs behind thick shields. Thick shields are becoming more relevant due to the increasing interest in long-term missions foreseen in the

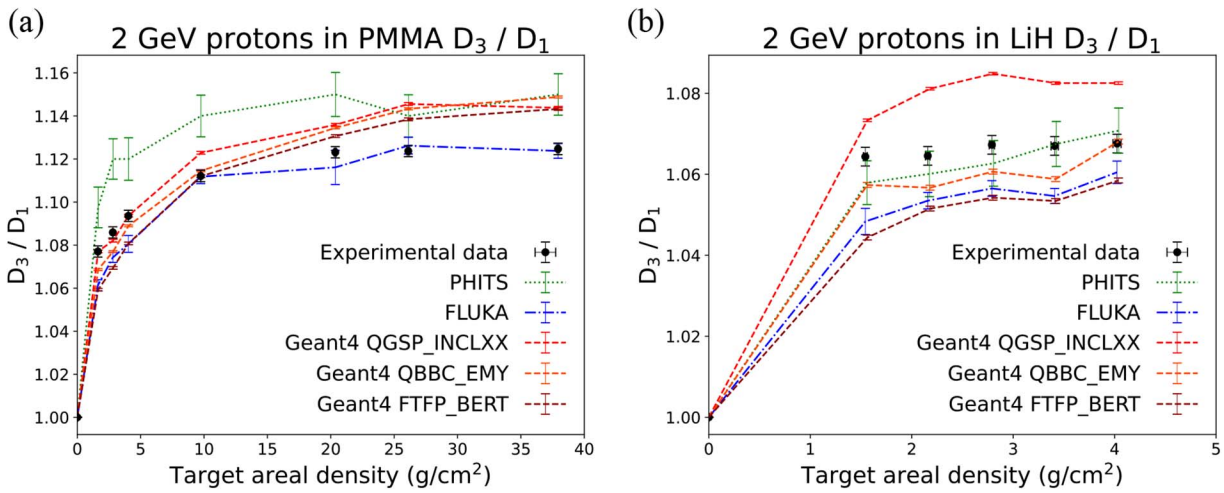

FIG. 9. Comparison between D_3/D_1 experimental data and Monte Carlo simulation results for PMMA and LiH irradiated with the 2 GeV ^{1}H beam.

next couple of decades, e.g., the mission to Mars or a Moon base. In all conditions, a significant dose build-up is observed in the first tens of g/cm^2 and it is to be attributed to nuclear fragmentation processes. This behavior is of interest because of the inverse shielding effect for light ions. It also allows the study of the impact of projectile and target fragmentation and provides valuable data for Monte Carlo benchmarking. All data were compared to Monte Carlo simulations. For the 2 GeV proton beam, three different simulation codes have been used, showing significant and systematic differences among codes that are used for the same radiation protection purposes. FLUKA fits the experimental data the best. Only FLUKA was used for the 480 MeV/u ^{1}H and 430 MeV/u ^{4}He beams and it showed good agreement. Although large ionization chambers were used, the limited available shielding material size showed a contribution of scattering effects, especially in the case of the LiH target. For the case of the Moon regolith simulant, discrepancies between the experimental data and FLUKA simulations also pointed out a Bragg peak broadening effect due to the granularity of the target material.

ACKNOWLEDGMENTS

This work was supported by ROSSINI3 (ESA Contract No. 4000125785/18/NL/GLC), which was a 2 year project started in December 2018, funded by ESA ESTEC and led by Thales Alenia Space Italia, and by DEIMOS, which is an ESA CORA (Continuously Open Research Announcement) funded project (Contract nr 4000134861/21/NL/PA/pt). The measurements performed in GSI Helmholtzzentrum für Schwerionenforschung in Darmstadt (Germany) Cave M were in the frame of FAIR Phase-0. MB acknowledges support from Project CH4.0, under the MUR program "Dipartimenti di Eccellenza 2023–2027" (CUP: D13C22003520001). The author would like to thank Brons Stephan and Scheloske Stefan for their support during the experiments at HIT.

Received: November 13, 2024; accepted: January 23, 2025; published online: February 10, 2025

REFERENCES

1. Managing Space Radiation Risk in the New Era of Space Exploration - National Research Council, Division on Engineering and Physical Sciences, Aeronautics and Space Engineering Board, Committee on the Evaluation of Radiation Shielding for Space Exploration. National Academies Press; 2008.
2. Durante M, Cucinotta FA. Physical basis of radiation protection in space travel. Rev Mod Phys 2011; 83(4):1245.
3. Cucinotta FA, Kim MHY, Chappell LJ, Huff JL. How safe is safe enough? Radiation risk for a human mission to Mars. PLoS One 2013; 8(10).
4. Chancellor JC, Scott GBI, Sutton JP. Space radiation: The number one risk to astronaut health beyond low earth orbit. Life (Basel) 2014; 4(3):491–510.
5. Kennedy AR. Biological Effects of Space Radiation and Development of Effective Countermeasures. Life Sci Space Res (Amst) 2014; 1(1):10.
6. Slaba TC, Bahadori AA, Reddell BD, Singleterry RC, Clowdsley MS, Blattnig SR. Optimal shielding thickness for galactic cosmic ray environments. Life Sci Space Res (Amst) 2017; 12:1–15.
7. Washburn SA, Blattnig SR, Singleterry RC, Westover SC. Active magnetic radiation shielding system analysis and key technologies. Life Sci Space Res (Amst) 2015; 4:22–34.
8. Miller J, Zeitlin C, Cucinotta FA, Heilbronn L, Stephens D, Wilson JW. Benchmark studies of the effectiveness of structural and internal materials as radiation shielding for the International Space Station. 2003; 159(3):381–90.
9. Shavers MR, Zapp N, Barber RE, Wilson JW, Qualls G, Toupes L, et al. Implementation of ALARA radiation protection on the ISS through polyethylene shielding augmentation of the Service Module Crew Quarters. Adv Space Res 2004; 34(6):1333–7.
10. Zeitlin C, Guetersloh SB, Heilbronn LH, Miller J. Measurements of materials shielding properties with 1 GeV/nuc 56Fe. Nucl Instrum Methods Phys Res B 2006; 252(2):308–18.
11. Guetersloh S, Zeitlin C, Heilbronn L, Miller J, Komiyama T, Fukumura A, et al. Polyethylene as a radiation shielding standard in simulated cosmic-ray environments. Nucl Instrum Methods Phys Res B 2006; 252(2):319–32.
12. Zeitlin C, La Tessa C. The role of nuclear fragmentation in particle therapy and space radiation protection. Front Oncol 2016; 6(MAR):180258.
13. Lobascio C, Briccarello M, Destefanis R, Faraud M, Gialanella G, Grossi G, et al. Accelerator-based tests of radiation shielding

properties of materials used in human space infrastructures. Health Phys 2008; 94(3):242–7.

14. Castellanos LA, McGirl NA, Srikrishna AP, Heilbronn L, La Tessa C, Rusek A, et al. Thick-target yields of secondary ions and neutrons for validation of radiation transport codes. IEEE Aerospace Conference Proceedings 2017 Jun 7.
15. Giraudo M, Schuy C, Weber U, Rovituso M, Santin G, Norbury JW, et al. Accelerator-based tests of shielding effectiveness of different materials and multilayers using high-energy light and heavy ions. Radiat Res 2018; 190(5):526–37.
16. Schuy C, Tessa C La, Horst F, Rovituso M, Durante M, Giraudo M, et al. Experimental assessment of lithium hydride's space radiation shielding performance and Monte Carlo benchmarking. Radiat Res 2019; 191(2):154–61.
17. Boscolo D, Scognamiglio D, Horst F, Weber U, Schuy C, Durante M, et al. Characterization of the secondary neutron field produced in a thick aluminium shield by 1 GeV/u 56Fe ions using TLD-based ambient dosimeters. Front Phys 2020; 8: 567142.
18. Luoni F, Boscolo D, Fiore G, Bocchini L, Horst F, Reidel CA, et al. Dose Attenuation in innovative shielding materials for radiation protection in space: Measurements and simulations. Radiat Res 2022; 198(2):107–19.
19. Zeitlin C, Guetersloh S, Heilbronn L, Miller J, Fukumura A, Iwata Y, et al. Fragmentation cross sections of medium-energy Cl35, Ar40, and Ti48 beams on elemental targets. Phys Rev C 2008; 77(3):034605.
20. Mancusi D, Bertucci A, Gialanella G, Grossi G, Manti L, Pugliese M, et al. Comparison of aluminum and lucite for shielding against 1GeV protons. Adv Space Res 2007; 40(4): 581–5.
21. La Tessa C, Guetersloh S, Heilbronn L, Miller J, Sihver L, Zeitlin C. Fragmentation of 1GeV/nucleon iron ions in thick targets relevant for space exploration. Ad Space Res 2005; 35(2): 223–9.
22. Badhwar GD, O'Neill PM. Galactic cosmic radiation model and its applications. Adv Space Res 1996; 17(2):7–17.
23. Slaba TC, Blattnig SR. GCR environmental models I: Sensitivity analysis for GCR environments. Space Weather 2014; 12(4): 217–24.
24. Norbury JW, Battistoni G, Besuglow J, Bocchini L, Boscolo D, Botvina A, et al. Are further cross section measurements necessary for space radiation protection or ion therapy applications? Helium projectiles. Front Phys 2020; 8:565954.
25. Peracchi S, Matsufuji N, Kok A, Povoli M, Jackson M, Rosenfeld AB, et al. A Solid-State Microdosimeter for Dose and Radiation Quality Monitoring for Astronauts in Space. IEEE Trans Nucl Sci. 2020; 67(1):169–74.
26. Peracchi S, James B, Psoroulas S, Grossmann M, Meer D, Bolst D, et al. Modelling of protons spectra encountered in space using medical accelerator and its microdosimetric characterization. Adv Space Res 2021; 67(8):2534–43.
27. Peracchi S, James B, Pagani F, Pan V, Vohradsky J, Bolst D, et al. Radiation shielding evaluation of spacecraft walls against heavy ions using microdosimetry. IEEE Trans Nucl Sci 2021; 68(5):897–905.
28. Pfuhl T, Horst F, Schuy C, Weber U. Dose build-up effects induced by delta electrons and target fragments in proton Bragg curves—measurements and simulations. Phys Med Biol 2018; 63(17):175002.
29. Carlsson CA, Carlsson GA. Proton dosimetry with 185 MeV protons. Dose buildup from secondary protons and recoil electrons. Health Phys (United Kingdom) 1977; 33:5.
30. Bertucci A, Durante M, Gialanella G, Grossi G, Manti L, Pugliese M, et al. Shielding of relativistic protons. Radiat Environ Biophys 2007; 46(2):107–11.
31. Yu Z, Vanstalle M, La Tessa C, Jiang GL, Durante M. Biophysical characterization of a relativistic proton beam for image-guided radiosurgery. J Radiat Res 2012; 53(4):620–7.
32. Di Chicco A, Boscolo D, Luoni F, Kozlova E, Weber U, Durante M, et al. Measurement of secondary neutron spectra induced by 480 MeV proton and 430 MeV/u ^{4} He beams with a thick aluminum target. J Instrum 2024; 19(01):C01035.
33. Ferrari A, Ranft J, Sala PR, Fassò A. FLUKA: A multi-particle transport code (program version 2005). Cern-2005-010. 2005; (October).
34. Vlachoudis V. FLAIR: a powerful but user friendly graphical interface for FLUKA. In: Proc Int Conf on Mathematics, Computational Methods & Reactor Physics (2009), Saratoga Springs, New York. 2009.
35. Böhlen TT, Cerutti F, Chin MPW, Fassò A, Ferrari A, Ortega PG, et al. The FLUKA Code: Developments and Challenges for High Energy and Medical Applications. Nuclear Data Sheets 2014; 120:211–4.
36. Battistoni G, Boehlen T, Cerutti F, Chin PW, Esposito LS, Fassò A, et al. Overview of the FLUKA code. Ann Nucl Energy 2015; 82:10–8.
37. Sato T, Iwamoto Y, Hashimoto S, Ogawa T, Furuta T, Abe SI, et al. Recent improvements of the particle and heavy ion transport code system – PHITS version 3.33. J Nucl Sci Technol 2024; 61(1):127–35.
38. Iwamoto Y, Hashimoto S, Sato T, Matsuda N, Kunieda S, Çelik Y, et al. Benchmark study of particle and heavy-ion transport code system using shielding integral benchmark archive and database for accelerator-shielding experiments. J Nucl Sci Technol 2022; 59(5):665–75.
39. Allison J, Amako K, Apostolakis J, Araujo H, Arce Dubois P, Asai M, et al. Geant4 developments and applications. IEEE Trans Nucl Sci 2006; 53(1):270–8.
40. Agostinelli S, Allison J, Amako K, Apostolakis J, Araujo H, Arce P, et al. Geant4—a simulation toolkit. Nucl Instrum Methods Phys Res A 2003; 506(3):250–303.
41. Allison J, Amako K, Apostolakis J, Arce P, Asai M, Aso T, et al. Recent developments in Geant4. Nucl Instrum Methods Phys Res A 2016; 835:186–225.
42. Aricò G, Schuy C, Horst F, Weber U, Ferrari A, Reidel CA, et al. Developments of the nuclear reaction and fragmentation models in FLUKA for ion collisions at therapeutic energies. CERN Proc 2019; 1:321–6.
43. Horst F, Schuy C, Weber U, Brinkmann KT, Zink K. Measurement of charge- and mass-changing cross sections for He4 + C12 collisions in the energy range 80–220 MeV/u for applications in ion beam therapy. Phys Rev C 2017; 96(2):024624.
44. Horst F, Aricò G, Brinkmann KT, Brons S, Ferrari A, Haberer T, et al. Measurement of He 4 charge- and mass-changing cross sections on H, C, O, and Si targets in the energy range 70-220 MeV/u for radiation transport calculations in ion-beam therapy. Phys Rev C 2019; 99(1):014603.
45. Horst F, Boscolo D, Durante M, Luoni F, Schuy C, Weber U. Thick shielding against galactic cosmic radiation: A Monte Carlo study with focus on the role of secondary neutrons. Life Sci Space Res (Amst) 2022; 33:58–68.
46. Boscolo D, Kostyleva D, Schuy C, Weber U, Haettner E, Purushothaman S, et al. Depth dose measurements in water for 11C and 10C beams with therapy relevant energies. Nucl Instrum Methods Phys Res A 2022; 1043:167464.
47. Horst F, Schardt D, Iwase H, Schuy C, Durante M, Weber U. Physical characterization of 3He ion beams for radiotherapy and comparison with 4He. Phys Med Biol 2021; 66(9): 095009.
48. Horst F, Ferrari A, Sala P, Schuy C, Durante M, Weber U. Precise measurement of the Bragg curve for 800 MeV/u 238U ions

stopping in polyethylene and its implications for calculation of heavy ion ranges. J Instrum 2022; 17(12):P12019.

49. Alica Karin Lang. Measurements and Simulations Using High-Energy Light Ions for Space Radiation Protection Applications. [Darmstadt]: Technische Universitaet Darmstadt; 2024.

50. Highland VL. Some practical remarks on multiple scattering. Nuc Instrum Meth 1975; 129(2):497–9.

51. Luoni F, Reidel CA, Horst F, Weber U, Durante M. Optimisation of the Tripathi model using a nuclear reaction cross-section database. New J Phys 2023; 25(12):123024.

52. Luoni F, Horst F, Reidel CA, Quarz A, Bagnale L, Sihver L, et al. Total nuclear reaction cross-section database for radiation protection in space and heavy-ion therapy applications. New J Phys 2021; 23(10):101201.